

Generalized Swift-Hohenberg models for dense active suspensions^{*,**}

Anand U. Oza^{1,a}, Sebastian Heidenreich², and Jörn Dunkel³

¹ Courant Institute of Mathematical Sciences, New York University, 251 Mercer Street, New York, NY 10012, USA

² Physikalisch-Technische Bundesanstalt Braunschweig und Berlin, Abbestr. 2-12, 10587 Berlin, Germany

³ Department of Mathematics, Massachusetts Institute of Technology, 77 Massachusetts Avenue, Cambridge, MA 02139-4307, USA

Received 20 April 2016 and Received in final form 23 August 2016

Published online: 25 October 2016 – © EDP Sciences / Società Italiana di Fisica / Springer-Verlag 2016

Abstract. In describing the physics of living organisms, a mathematical theory that captures the generic ordering principles of intracellular and multicellular dynamics is essential for distinguishing between universal and system-specific features. Here, we compare two recently proposed nonlinear high-order continuum models for active polar and nematic suspensions, which aim to describe collective migration in dense cell assemblies and the ordering processes in ATP-driven microtubule-kinesin networks, respectively. We discuss the phase diagrams of the two models and relate their predictions to recent experiments. The satisfactory agreement with existing experimental data lends support to the hypothesis that non-equilibrium pattern formation phenomena in a wide range of active systems can be described within the same class of higher-order partial differential equations.

1 Introduction

A key feature of unicellular and multicellular organisms is the emergence of characteristic length scales that are set by a combination of biochemical and physical processes [1,2]. Cells divide when they reach roughly the same critical size or volume [3]; embryos develop highly reproducible folding and buckling patterns [4]; human individuals possess nearly identical organs; and many animals such as zebras, fish and butterflies possess color patterns of a well-defined scale. Such pattern formation phenomena can be naturally modeled in Fourier space [2]. For a dynamical process that selects a pattern of a certain length scale Λ , the corresponding Fourier-transformed dynamics amplifies the modes of corresponding wave number $k_\Lambda = 2\pi/\Lambda$. This suggests that partial differential equations (PDEs) of spatial order greater than two can provide a generic and efficient framework for describing biological and other natural pattern selection processes [2].

* Contribution to the Topical Issue “Nonequilibrium Collective Dynamics in Condensed and Biological Matter”, edited by Holger Stark, Marcus Baer, Carsten Beta, Sabine Klapp and Andreas Knorr.

** Supplementary material in the form of eight .mov files available from the Journal web page at

<http://dx.doi.org/10.1140/epje/i2016-16097-2>

^a e-mail: oza@cims.nyu.edu

To illustrate this idea in more detail, consider a hypothetical system described by a field $\phi(t, \mathbf{x})$, which may represent a gene expression profile, molecular concentration, color, or any other relevant scalar quantity describing a collection of cellular components, cells or organisms. In general, the dynamics of $\phi(t, \mathbf{x})$ and its associated Fourier modes $\hat{\phi}(t, \mathbf{k})$ is highly nonlinear, but some progress is often achieved by approximating the full dynamics through Taylor expansions. For instance, suppose that the configurations $\pm\phi$ are equally likely to occur, and that the characteristic “color” values $\pm\phi_c$ are preferred. We would then expect the leading order dynamics to have the form

$$\partial_t \phi = a\phi + b\phi^3 + \dots, \quad (1)$$

where $\phi_c = \sqrt{-a/b}$ with $a > 0$ and $b < 0$ to ensure stability of the fixed points $\pm\phi_c$. Similarly, when patterns of length scale Λ (corresponding to wavemodes $k_\Lambda = 2\pi/\Lambda$) are selected in an otherwise isotropic spatial setting, we would expect the leading order dynamics in Fourier space to have the form

$$\partial_t \hat{\phi} = (\alpha|\mathbf{k}|^2 + \beta|\mathbf{k}|^4 + \dots)\hat{\phi}, \quad (2)$$

where $k_\Lambda = \sqrt{-\alpha/(2\beta)}$ with $\alpha > 0$ and $\beta < 0$ to ensure that small-wavelength modes decay, or $\hat{\phi}(t, \mathbf{k}) \rightarrow 0$ as $|\mathbf{k}| \rightarrow \infty$. We may thus combine eqs. (1) and (2) and

obtain the following PDE in position space:

$$\partial_t \phi = a\phi + b\phi^3 - \alpha \nabla^2 \phi + \beta (\nabla^2)^2 \phi. \quad (3)$$

Intuitively, the field's observed "colors" or values are identified with fixed points of eq. (1), while the length scale of the most prevalent pattern corresponds to the Fourier mode with maximal growth rate in eq. (2). Equations (1) and (2) may be generalized by considering more general expansions in both position and Fourier space, the latter of which might introduce pseudo-differential operators to eq. (3), but such extensions do not affect the general idea.

Although the arguments leading to eq. (3) are purely formal, continuum equations of this type have been derived from more fundamental models in a few select cases [5,6]. A well-known example is the celebrated Swift-Hohenberg theory [5] of Rayleigh-Benard convection in a heated fluid. More recently, it was shown that surface pattern formation processes in curved elastic bilayer materials can be described by a fourth-order PDE of the same type [6]. Furthermore, phenomenological models resembling (3) have been successfully applied to describe pattern formation processes in granular media [7]. The applicability of these ideas to the collective non-equilibrium dynamics of biological systems has not been thoroughly investigated, but there is some encouraging preliminary evidence [8–10]. In this contribution, we compare two models that generalize eq. (3) to vector fields and matrix fields. The vector model aims to describe polar cell motility in dense microbial suspensions [8,9], whereas the matrix field theory is designed to capture apolar orientational order in concentrated ATP-driven microtubule-kinesin suspensions [10–12].

Specifically, the discussion of the vector model in sect. 2 focuses on systems consisting of microscopic constituents that exhibit intrinsic geometric [13,14] or kinematic polarity [15,16], such as bacteria or sperm cells, for which the position of the flagellum relative to the cell body defines an orientation vector. For assemblies of $\sigma = 1, \dots, N$ polar objects with individual orientations \mathbf{n}_σ , we can define the mean local orientation field $\mathbf{p}(t, \mathbf{x}) = \langle \mathbf{n}_\sigma \rangle_{(t, \mathbf{x})}$, where the average is taken over a small volume enclosing the space point \mathbf{x} at time t . In contrast, the field \mathbf{p} is not a meaningful order parameter for front-back symmetric rod-like particles, called nematics, since \mathbf{n}_σ and $-\mathbf{n}_\sigma$ are equally valid characterizations of the same particle and thus $\mathbf{p}(t, \mathbf{x}) \equiv 0$ by symmetry. Instead, a non-trivial characterization of nematics can be given in terms of the second-moment matrix-field $Q(t, \mathbf{x}) = \langle \mathbf{n}_\sigma \mathbf{n}_\sigma \rangle_{(t, \mathbf{x})} - \mathbf{I}/d$, where \mathbf{I} is the d -dimensional identity matrix. Note that, by construction, Q is symmetric and traceless, $\text{Tr}[Q] = \sum_{i=1}^d Q_{ii} = 0$. The matrix model in sect. 3 applies to systems that comprise approximately front-back symmetric particles without an intrinsically preferred direction of motion but which collectively achieve complex dynamics, for example by creating advective hydrodynamic flows [11,12,17]. We here restrict our attention to the two-dimensional case $d = 2$, which is of relevance to the motion of both cells and microtubule bundles on or near solid surfaces.

2 Vector field theory for polar cells

In the past decade, bacterial and other active suspensions [8,18–28] have emerged as important biophysical model systems characterized by mesoscale spatio-temporal pattern formation from microscopic non-equilibrium dynamics [29–41]. Highly concentrated motile bacteria spontaneously organize into mesoscopic jet [21] and vortex structures, spanning several cell lengths in diameter [8,9,25] and persisting for several seconds [9] or even minutes [42–45]. A conceptually simple continuum model, accounting both qualitatively and quantitatively for the experimental observations [8,9], is obtained [46] by merging the seminal Toner-Tu flocking theory [47–49] with the Swift-Hohenberg theory of pattern formation [5] as follows. Focusing on the incompressible high-density regime in which bacterial concentration fluctuations are negligible, we consider the generic transport law for the local mean orientation vector field $\mathbf{p}(t, \mathbf{x})$ of the cells,

$$(\partial_t + \mathbf{u} \cdot \nabla) \mathbf{p} = -\frac{\delta \mathcal{G}}{\delta \mathbf{p}}, \quad (4)$$

where $\mathbf{u}(t, \mathbf{x})$ is the transport velocity field and \mathcal{G} the effective non-equilibrium free energy. If cells move primarily in the direction of their orientation, the velocity field may be approximated as proportional to the orientation vector field,

$$\mathbf{u} = \lambda_0 \mathbf{p}, \quad (5)$$

with mass (or number) conservation implying the incompressibility constraint $\nabla \cdot \mathbf{u} = \nabla \cdot \mathbf{p} = 0$. Equation (5) is a reasonable approximation for sufficiently "dry" polar active matter. This class includes truly dry systems such as vibrated granular media with broken front-back symmetry, microbial suspensions on surfaces that suppress hydrodynamic effects [8] or, more generally, situations in which self-propulsion dominates hydrodynamics. If fluid flows play a dominant role, additional terms accounting for coupling to fluid vorticity and strain must be included in the transport law (4) [35].

To obtain a closed model for \mathbf{p} , we still need to specify the free energy \mathcal{G} . Assuming that cells prefer to align their orientations locally, we consider the generic ansatz [46]

$$\mathcal{G} = \int d^2x \left[-q(\nabla \cdot \mathbf{p}) - \frac{\alpha}{2} \mathbf{p}^2 + \frac{\beta}{4} \mathbf{p}^4 + \frac{\Gamma_0}{2} (\nabla \mathbf{p})^2 + \frac{\Gamma_2}{2} (\nabla \nabla \mathbf{p})^2 \right], \quad (6)$$

where the scalar pressure field $q(t, \mathbf{x})$ is the local Lagrange multiplier for the incompressibility constraint, $(\nabla \mathbf{p})^2 = (\partial_i p_j)(\partial_i p_j)$ and $(\nabla \nabla \mathbf{p})^2 = (\partial_i \partial_j p_k)(\partial_i \partial_j p_k)$, summation over repeated indices $i, j, k = 1, 2$ being implied. As in eq. (3), the last four terms in eq. (6) may be interpreted as the leading-order terms of a generic Taylor expansion in both order-parameter space and Fourier space. Thus, the resulting fourth-order model can be written as

$$\nabla \cdot \mathbf{p} = 0, \quad (7a)$$

$$(\partial_t + \lambda_0 \mathbf{p} \cdot \nabla) \mathbf{p} = -\nabla q + (\alpha - \beta |\mathbf{p}|^2) \mathbf{p} + \Gamma_0 \nabla^2 \mathbf{p} - \Gamma_2 (\nabla^2)^2 \mathbf{p}, \quad (7b)$$

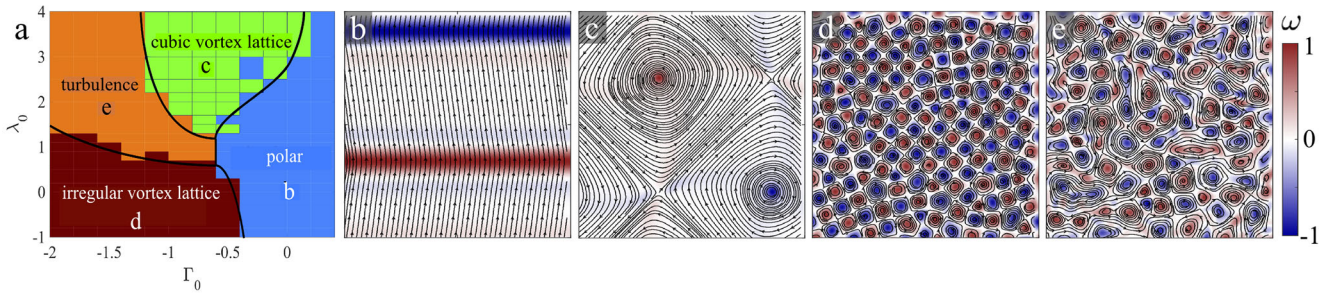


Fig. 1. Simulations of the vector model (7) for various values of the orientational diffusivity parameter Γ_0 and self-advection parameter λ_0 , using random initial conditions and simulation box size $L = 24\pi$. (a) Phase diagram showing the dependence of the simulated long-time dynamics on Γ_0 and λ_0 . (b)–(e) Still images from representative simulations, the arrows showing streamlines of the velocity field \mathbf{u} and the color bar indicating the orientational vorticity $\omega = \epsilon_{ij}\partial_i p_j$ normalized by its maximum absolute value. We observe polar states (panel b), cubic vortex lattices (panel c, Supplementary Movie 1), irregular vortex lattices (panel d, Supplementary Movie 2), and turbulent states (panel e, Supplementary Movie 3). The simulation parameters are (b) $\Gamma_0 = 0$, $\lambda_0 = 2$; (c) $\Gamma_0 = -0.6$, $\lambda_0 = 4$; (d) $\Gamma_0 = -1.2$, $\lambda_0 = 0$; and (e) $\Gamma_0 = -2$, $\lambda_0 = 2.5$.

where $(\lambda_0, \alpha, \beta, \Gamma_0, \Gamma_2)$ are phenomenological parameters that can be determined by fitting numerical solutions of eqs. (7) to experimental data [8, 9], analogous to the viscosity in the classical Navier-Stokes equations of hydrodynamics [50]. As in the Toner-Tu flocking model [47–49], the parameters $\alpha, \beta > 0$ describe effective polar alignment similar to that induced by ferromagnetic spin interactions. Equation (7b) has an unstable isotropic fixed point $\mathbf{p} = 0$ and a manifold of stable fixed points with $|\mathbf{p}| = \sqrt{\alpha/\beta}$, corresponding to a globally ordered polar state with arbitrary uniform orientation. The Swift-Hohenberg-type spatial derivative terms with coefficients Γ_0 and Γ_2 determine the length and time scale of typical patterns when $\Gamma_0 < 0$. Short-wavelength stability, or equivalently well-posedness, of the theory requires that $\Gamma_2 > 0$, but the orientational “diffusion” parameter Γ_0 can have either sign. For $\Gamma_0 > 0$, the system is damped into a stable homogeneous polar state [46]. By contrast, for $\Gamma_0 < 0$, these states destabilize into patterns with characteristic length $\Lambda \sim \sqrt{\Gamma_2/(-\Gamma_0)}$ and lifetime $\tau \sim \Gamma_2/\Gamma_0^2$, as suggested by dimensional considerations. Analysis of a microscopic model of polar swimmers showed that Γ_0 may become negative when the volume fraction, self-propulsion speed and force density of the active swimmers are sufficiently large [51].

To solve eqs. (7) numerically, we implemented a pseudospectral algorithm using periodic boundary conditions in space and an operator-splitting Euler method for time integration [8, 46], with 128 lattice points in each spatial direction and time step $\Delta t = 10^{-2}$. After rescaling to dimensionless coordinates, which is equivalent to setting $\alpha = \beta = \Gamma_2 = 1$, the remaining model parameters are (λ_0, Γ_0) and the simulation box size L . The dimensionless self-advection parameter λ_0 plays the role of an effective Reynolds number. A numerically determined phase diagram in the (λ_0, Γ_0) -parameter plane using random initial conditions and representative still images from long-time runs are shown in fig. 1. If $|\lambda_0|$ is subcritical, ordered polar states or vortex-lattice patterns form (figs. 1b and d). For supercritical values of λ_0 , these patterns become mixed

by the nonlinear advection term and thus generate a turbulent state, an effect that is amplified by the two-dimensional incompressibility constraint in eq. (7a) [52]. In the intermediate regime $-1.25 < \Gamma_0 < -0.75$, there is a transition from turbulence (fig. 1e) to a cubic vortex lattice (fig. 1c) of large vortices as λ_0 is progressively increased. This may be due to the inverse energy cascade in 2D turbulence, which transports energy from small to large scales [52, 53], and to the finite size of our simulation box. While the orientational diffusion term proportional to Γ_0 is responsible for the formation of small-scale vortices (fig. 1d–e), the advection term becomes more important above a critical value of λ_0 , and the large vortices characteristic of the cubic lattice phase appear. Decreasing Γ_0 to large negative values for fixed λ_0 generally favors lattice-like states (fig. 1c–e). We note that similar vortex-lattice states were predicted in [54], who considered a more complex hydrodynamic model for active polar gels and assessed the linear stability of the homogenous polar state. Ordered vorticity patterns have also been observed in experiments on dividing endothelial cells, and a continuum model inspired by eqs. (7) was used to reproduce the key experimental observations [55].

It has been shown that eqs. (7) reproduce the key statistical features observed in experiments using dense quasi-2D [8] and quasi-3D [9] *B. subtilis* suspensions confined in microfluidic channels. In particular, the corresponding kinetic energy spectra exhibit a characteristic peak [8] at the wave number corresponding to the typical vortex size. Such peaks constitute a hallmark of mesoscale turbulence and are in stark contrast to the scale-free power-law spectra in classical high Reynolds number turbulence [50, 52]. The presence of spectral peaks in bacterial mesoscale turbulence lends support to the idea that important characteristics of active polar suspensions may be understood in terms of universal free energy expansions of the form (6). Recently, more progress has been made in understanding how the active turbulence predicted by eqs. (7) differs quantitatively from classical turbulence [56].

3 Matrix field theory for 2D active liquid crystals

Two-dimensional active liquid crystal (ALC) analogs [12, 17, 57–60] comprise another class of non-equilibrium systems that lends itself to quantitative tests of generic pattern-formation concepts [61]. ALCs are assemblies of approximately rod-like particles that develop non-thermal collective excitations due to steady external [57, 58] or internal [12, 17] energy input. At high concentrations, both dry and wet ALCs form an active nematic phase characterized by dynamic creation and annihilation of topological defects [12, 17, 57]. This phenomenon was observed recently in suspensions of ATP-driven microtubule-kinesin bundles that were trapped in a flat oil-water interface [11, 12] or near the curved surface of a vesicle [17]. As outlined in sect. 1, orientational order in such active nematics can be naturally described in terms of the matrix field $Q(t, \mathbf{x})$ which describes the local second statistical moment of the particle orientation distribution.

Over the past decade, several nematic order-parameter models [34, 62–67] and kinetic theories [68] for wet [12, 17] and dry ALC systems [57, 58] have been proposed and derived, although most of them still need to be tested quantitatively against experimental data. We here consider the recent experiments on wet ALCs [11, 12] and aim to describe the orientational order of ATP-driven microtubule-kinesin filaments at a planar oil-water interface close to a solid boundary (distance $\sim 3 \mu\text{m}$). To this end, we consider a compact minimal model that generalizes the vector model from eqs. (7) to the symmetric traceless 2×2 -matrix field Q [10], starting again from a generic transport law for a hydrodynamically advected tensor field:

$$\partial_t Q + \nabla \cdot (\mathbf{u}Q) - \kappa[Q, \Omega] = -\frac{\delta \mathcal{F}}{\delta Q}, \quad (8)$$

where $\Omega = [\nabla \mathbf{u} - (\nabla \mathbf{u})^\top]/2$ is the vorticity tensor of the 2D interfacial flow \mathbf{u} with coupling parameter $\kappa = 1$ for passive LCs, $[A, B] = AB - BA$ the matrix commutator and \mathcal{F} an effective free energy. The scalar nematic order-parameter $S(t, \mathbf{x}) = \sqrt{\text{Tr}[2Q^2]}$ is proportional to the larger eigenvalue of Q , and the filaments are oriented along the corresponding eigenvector, or director $\mathbf{d}(t, \mathbf{x})$. Focusing on dense suspensions as realized in the experiments [11, 12], we neglect fluctuations in the microtubule concentration. Additional terms that model microtubule alignment with the flow may also be added, examples being $\{Q, E\}$ [66, 67] and SE [65], where $\{A, B\} = AB + BA$ is the matrix anticommutator and $E = [\nabla \mathbf{u} + (\nabla \mathbf{u})^\top]/2$ the strain rate tensor. We neglect these here in the interest of constructing a minimal theory capable of capturing the key experimental observations. It is important, however, that $\nabla \cdot (\mathbf{u}Q) \neq \mathbf{u} \cdot \nabla Q$ when $\nabla \cdot \mathbf{u} \neq 0$, which is typically the case when fluid can enter and leave the interface.

The 2D flow field \mathbf{u} may be related to Q through the damped Stokes equation [69]

$$-\mu \nabla^2 \mathbf{u} + \nu \mathbf{u} = -\zeta \nabla \cdot Q, \quad (9)$$

where μ is the viscosity and the rhs. represents active stresses [64, 70], with $\zeta > 0$ ($\zeta < 0$) for extensile (contractile) ALCs. The ν -term describes effective friction from a nearby no-slip boundary [11, 12] in the Hele-Shaw approximation [69]. A straightforward boundary-layer scaling argument suggests that ν scales with the distance h from the boundary as $\nu \propto h^{-\eta}$ where $\eta \in [1, 2]$. In the overdamped regime $\nu \Lambda^2/\mu \gg 1$, where Λ is the length scale of typical patterns in the active nematics, eq. (9) reduces to

$$\mathbf{u} = -\lambda_0 \nabla \cdot Q, \quad \lambda_0 = \zeta/\nu. \quad (10)$$

Inserting the closure condition (10) into (8) yields a closed Q -theory, once we have specified the effective free energy \mathcal{F} . Combining Landau-de Gennes theory [71] with Swift-Hohenberg theory [5], a generic ansatz for the free energy resembling eq. (6) is given by¹

$$\mathcal{F} = \int d^2x \left\{ -\frac{\alpha}{2} \text{Tr}[Q^2] + \frac{\beta}{4} \text{Tr}[Q^4] + \frac{\Gamma_0}{2} (\nabla Q)^2 + \frac{\Gamma_2}{4} (\nabla \nabla Q)^2 \right\}, \quad (11)$$

where $\alpha, \beta > 0$ for the nematic phase, $(\nabla Q)^2 = (\partial_k Q_{ij})(\partial_k Q_{ij})$ and $(\nabla \nabla Q)^2 = (\partial_k \partial_l Q_{ij})(\partial_k \partial_l Q_{ij})$. Assuming that Γ_0 can have either sign, short-wavelength stability requires that $\Gamma_2 > 0$. The free energy \mathcal{F} possesses a homogeneous nematic ground-state manifold for $\Gamma_0 > 0$, whereas a pattern of characteristic wavelength $\Lambda \sim \sqrt{\Gamma_2/(-\Gamma_0)}$ becomes energetically favorable for $\Gamma_0 < 0$.

The choice $\Gamma_0 < 0$ has an intrinsically microscopic origin, as it describes kinesin-driven microtubule bundles that undergo spontaneous buckling. This is caused by the the motor-induced extensile shear dynamics of adjacent bundles (fig. 1c in ref. [12]), an extended discussion of which is given in ref. [10]. To summarize, the ALC assembly consists of microtubules that grow against each other and spontaneously buckle. Previous work has shown that individual microtubules can couple to their surrounding network and spontaneously buckle under compressive stresses [72], which here are effectively generated by their motor-induced extensile shear. This is in contrast to passive LCs, for which $\Gamma_0 > 0$ in the free energy causes spatial inhomogeneities in the director field to be penalized. We note that hydrodynamic effects could also lead to microtubule buckling [66, 73], but believe this to be a secondary effect. Indeed, fig. 1d in ref. [12] shows a scale separation between microtubule buckling and hydrodynamic flow structures in the isotropic phase at low microtubule concentrations, which suggests that hydrodynamic coupling is not necessary to generate spontaneous microtubule buckling.

We note that eq. (11) is the formal generalization of eq. (6) to matrix fields. However, a subtle yet important difference is due to the compressibility of the 2D velocity field, $\nabla \cdot \mathbf{u} \neq 0$, reflecting that, in the experiments [11, 12],

¹ Note that ref. [10] uses a different sign convention for the parameter multiplying the $(\nabla Q)^2$ term in eq. (11).

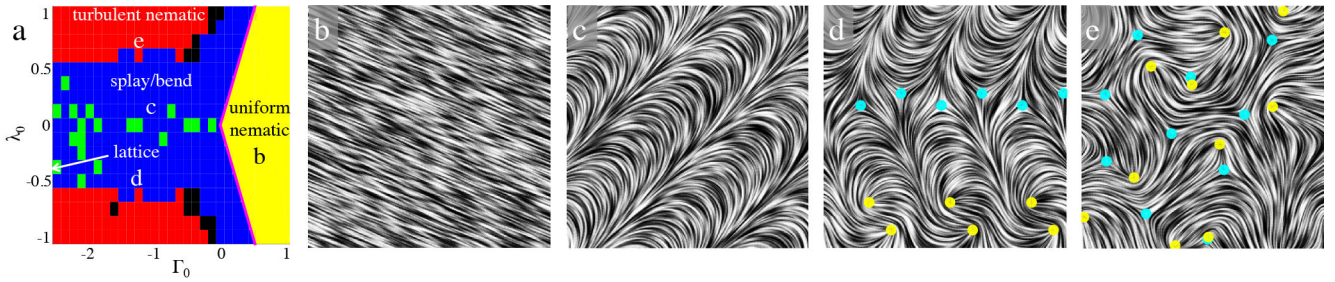


Fig. 2. Simulations of the matrix model (12) for various values of the orientational diffusion parameter Γ_0 and self-advection parameter λ_0 , using random initial conditions and simulation box size $L \geq 6\pi$. The vorticity coupling parameter $\kappa = 1$ throughout. (a) Phase diagram showing the dependence of the simulated long-time dynamics on Γ_0 and λ_0 . The pink curve indicates the stability boundary $|\lambda_0| = 2\Gamma_0$ for the uniformly aligned nematic state, based on the linear stability analysis outlined in appendix A (fig. 3c). (b)–(e) Representative still images from the simulations, the nematic director field $\mathbf{d}(\mathbf{x})$ being rendered using line integral convolution. Topological defects are identified using the method described in ref. [10], and indicated in yellow ($+\frac{1}{2}$) and blue ($-\frac{1}{2}$). We observe uniformly aligned states (yellow, panel b), static or oscillatory defect-free splay/bend states (blue, panel c, Supplementary Movies 4 and 8), long-lived static or oscillatory defect lattice states (green, panel d, Supplementary Movie 6) and turbulent nematic states (red, panel e, Supplementary Movie 7) characterized by spontaneous topological defect creation and annihilation. We also observe states characterized by oscillatory defect creation and annihilation events (black, Supplementary Movie 5). The dimensionless simulation parameters are (b) $\lambda_0 = -0.625$, $\Gamma_0 = 1$; (c) $\lambda_0 = 0.375$, $\Gamma_0 = -1.5$; (d) $\lambda_0 = -0.375$, $\Gamma_0 = -2.5$; and (e) $\lambda_0 = 1$, $\Gamma_0 = -1$.

microtubules assemble at an interface layer which can continuously exchange fluid with the environment. Inserting the hydrodynamic closure condition (10) and the free energy ansatz (11) into eq. (8), we obtain

$$\begin{aligned} \partial_t Q - \lambda_0 \nabla \cdot [(\nabla \cdot Q)Q] - \kappa[Q, \Omega] = \\ \alpha Q - \beta Q^3 + \Gamma_0 \nabla^2 Q - \Gamma_2 (\nabla^2)^2 Q. \end{aligned} \quad (12)$$

As in sect. 2, eq. (12) can be rewritten in a dimensionless form that is equivalent to setting $\alpha = \beta = \Gamma_2 = 1$, thus leaving (λ_0, Γ_0) as the only two relevant parameters.

To solve the resulting dimensionless equation, we implemented a pseudospectral algorithm with periodic boundary conditions in space and a modified exponential time differencing fourth-order Runge-Kutta time-stepping scheme [74]. Simulations were performed with time step $\Delta t \leq 2^{-10}$ and at least 256 lattice points in each spatial direction. The simulations conducted here extend the results of ref. [10] by incorporating the vorticity coupling term ($\kappa = 1$), and exploring the parameter regimes $\Gamma_0 > 0$ and $\lambda_0 < 0$, which corresponds to contractile active nematics. While the experiments in refs. [11, 12] were done using extensile nematics, for which $\lambda_0 > 0$ and $\Gamma_0 < 0$, we here explore the entire (λ_0, Γ_0) parameter space to obtain a complete characterization of the model (12). It is evident from eq. (10) that the limit $\lambda_0 \rightarrow 0$ corresponds to decreasing the activity parameter ζ or increasing the effective boundary friction ν . We here consider the latter scenario, which could be achieved experimentally by decreasing the depth of the ALC layer, using the setup described in ref. [75].

A numerically obtained phase diagram of eq. (12) for random initial conditions $Q(0, \mathbf{x})$ is shown in fig. 2a, along with representative still images from the simulations in fig. 2b–e. It is evident that the uniformly aligned state (fig. 2b) is stable for sufficiently large values of the orientational diffusion parameter Γ_0 , specifically, in the re-

gion $\Gamma_0 > |\lambda_0|/2$, which is in agreement with the results of the linear stability analysis of the uniform state presented in appendix A (fig. 3c). Spatially periodic defect-free splay/bend states (fig. 2c) are prevalent for moderate values of the self-advection parameter λ_0 , although we also observe a number of other more complex phases. For relatively small values of Γ_0 , we observe oscillatory states in which the nematic undergoes oscillations in a defect-free environment (Supplementary Movie 4). The system may also exhibit relaxation oscillations, which consist of long periods in which the the director is nearly uniformly aligned, followed by rapid bursts in which the director rotates by 90 degrees (Supplementary Movie 8). This state was observed in the multi-field active nematic model analyzed in ref. [76]. We also observe oscillatory states characterized by the spontaneous creation and annihilation of topological defects (Supplementary Movie 5).

As Γ_0 becomes more negative, we observe more long-lived static or oscillatory defect lattice states (fig. 2d, Supplementary Movie 6), in which the topological defects are found in an ordered arrangement. The long-lived states are related to the “vortex lattices” observed by simulating a multi-field active nematic model that allows for variations in the microtubule concentration, but assumes that $\Gamma_0 > 0$ [67]. These vortex lattices consist of an ordered arrangement of topological defects in which $+\frac{1}{2}$ -defects remain between counter-rotating vortices, as also observed in our simulations (see fig. 3 in ref. [10]). Such ordered arrangements were reported in ref. [67] for both extensile ($\lambda_0 > 0$) and contractile ($\lambda_0 < 0$) nematics, in agreement with our simulations (fig. 2a).

For larger values of λ_0 , the system evolves into a turbulent nematic state (fig. 2e, Supplementary Movie 7) characterized by an aperiodic dynamics with spontaneous creation and annihilation of topological defects. We observe that the dynamics for small values of λ_0 is sensitive to the initial conditions, and that multiple long-lived configura-

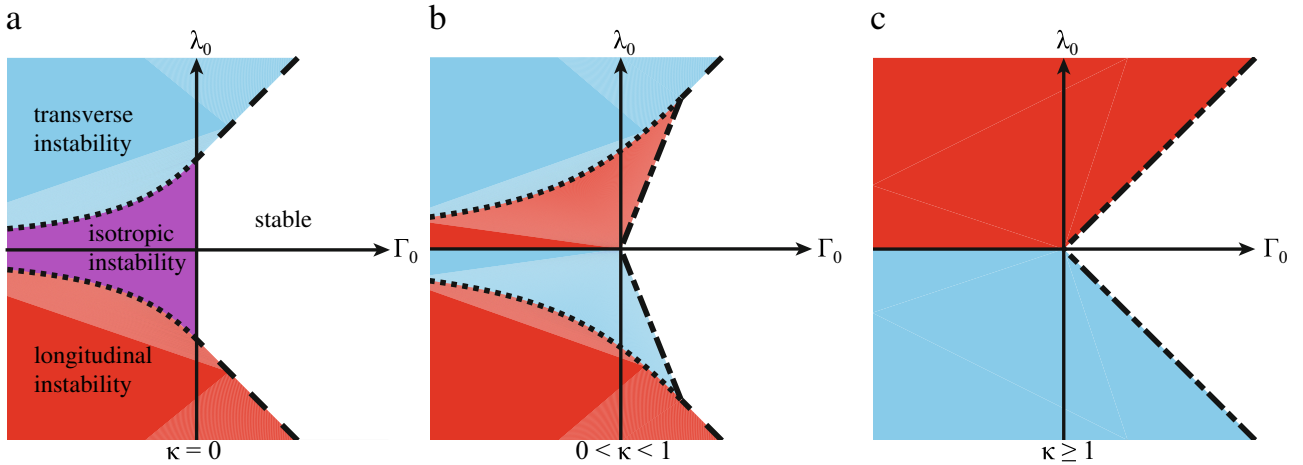


Fig. 3. Results of the linear stability analysis of the uniformly aligned state in the (Γ_0, λ_0) plane, for (a) $\kappa = 0$, (b) $0 < \kappa < 1$ and (c) $\kappa \geq 1$. The uniform state is stable in the white regions; it undergoes an isotropic instability in the violet region, a longitudinal instability along the director field in the red regions, and a transverse instability perpendicular to the director field in the blue regions. The dashed curves correspond to $|\lambda_0| = 2(\Gamma_0 + \sqrt{2})$, the dotted curves to $|\lambda_0| = \frac{2}{1+\kappa}(\Gamma_0 + \sqrt{\Gamma_0^2 + \frac{2(1+\kappa)}{1-\kappa}})$, and the dashed-dotted curve to $|\lambda_0| = 2\Gamma_0/\kappa$.

tions may exist for a given set of parameter values. We also note that, while the self-advection term with prefactor λ_0 breaks the $\mathbf{p} \rightarrow -\mathbf{p}$ symmetry of the vector model (7) and the $Q \rightarrow -Q$ symmetry of the tensor model (12), only the phase diagram for the tensor model is approximately symmetric with respect to λ_0 .

As demonstrated in ref. [10], the two-parameter model (12) correctly reproduces the spontaneous creation and subsequent dynamics of $\pm\frac{1}{2}$ defect pairs, while also accounting quantitatively for their speed and lifetime distributions. Furthermore, eq. (12) predicts a regime characterized by antipolar ordering of $+\frac{1}{2}$ -defect orientations. This is in contrast to the polar ordering of $+\frac{1}{2}$ -defects observed in Brownian dynamics simulations of rigid rods that grow, divide, and merge in the absence of hydrodynamic interactions [11]. Physically, the lattice states (fig. 2d) observed at low values of the self-advection parameter λ_0 destabilize into a chaotic dynamics as λ_0 is increased, but the defect orientational order persists within a neighborhood of several defects. Orientational order of topological defects was also observed in recent experiments [11]. Similar to the long-lived lattice states observed in our simulations of eq. (12), the experiments exhibited system-spanning nematic ordering of $+\frac{1}{2}$ -defects. However, this regime was realized experimentally while the defects exhibited a complex and presumably chaotic dynamics.

Previous models for ALCs assumed an incompressible 2D flow field \mathbf{u} , thus neglecting both fluid transfer between interface and bulk, and friction from nearby boundaries. We note that the incompressibility assumption artificially induces large-scale mixing through a turbulent upward cascade, analogous to that in classical 2D hydrodynamic turbulence [52, 53]. In 2D microtubule-kinesin layers [11, 12], flow is generated by the spatial gradi-

ents of Q , as described in eq. (9). The largest gradients occur in the vicinity of topological defects; that is, these defects effectively stir the fluid on small scales. In a truly incompressible 2D fluid, potentially realizable with a soap-film setup [77], such small-scale energy input would be transported to larger scales through an upward cascade [52, 53]. Under the recently realized experimental conditions [11, 12], however, an upward cascade is suppressed by damping and fluid exchange between the ALC layer and bulk. The model (12) implicitly accounts for these effects and hence predicts that topological defects remain locally ordered despite evolving via a chaotic dynamics [10]. Generally, this example demonstrates that effective 2D hydrodynamic descriptions of 3D active systems must be handled with care.

4 Conclusions

We have illustrated how nonlinear fourth-order vector and matrix continuum models can provide a useful quantitative description of collective cell migration [8, 9] and ATP-driven microtubule-kinesin suspensions [10]. Conceptually, eqs. (6) and (11) build directly on “universality” ideas in pattern formation [5, 7] by simply assuming the validity of leading-order expansions in both order-parameter space and Fourier space. The fact that such a generic approach has proved successful for three vastly different classes of systems [6, 8–10] lends support to the hypothesis [61] that the pattern formation dynamics in soft active matter systems is governed by generic ordering principles. An important next step towards further validation is to derive such higher-order equations from microscopic models [33].

This work was supported by the NSF Mathematical Sciences Postdoctoral Research Fellowship DMS-1400934 (A.O.), an MIT Solomon Buchsbaum Fund Award (J.D.) and an Alfred P. Sloan Research Fellowship (J.D.). The authors would like to thank Zvonimir Dogic, Stephen DeCamp, Michael Hagan, Ken Kamrin, Mehran Kardar, Jonasz Słomka, Norbert Stoop and Francis Woodhouse for insightful discussions.

Appendix A.

We here consider the linear stability of the uniform state

$$Q = Q_0 \equiv \frac{1}{2} \begin{pmatrix} \cos 2\theta & \sin 2\theta \\ \sin 2\theta & -\cos 2\theta \end{pmatrix},$$

in which the nematic director field is uniformly aligned with fixed angle θ . This analysis extends the results presented in the Supplementary Material of ref. [10] to the parameter regime $\lambda_0 < 0$. We substitute $Q = Q_0 + \epsilon \hat{Q}(t) e^{i\mathbf{k}\cdot\mathbf{x}}$ into eq. (12), non-dimensionalized so that $\alpha = \beta = \Gamma_2 = 1$, and retain terms at order ϵ . As shown in ref. [10], the maximal eigenvalue of the linear stability problem has the form

$$\sigma(k, u) = -\Gamma_0 k^2 - k^4 + \frac{1}{4} \left[-1 - \lambda_0(1 - \kappa)k^2 u + \sqrt{(1 + \lambda_0(1 + \kappa)k^2 u)^2 + 4\lambda_0^2 \kappa k^4 (1 - u^2)} \right],$$

where $\mathbf{k} = k(\cos \phi, \sin \phi)$ and $u = \cos[2(\phi - \theta)]$. A straightforward generalization of the argument in ref. [10] shows that, for $\lambda_0 < 0$,

$$\sigma^*(k) \equiv \max_{-1 \leq u \leq 1} \sigma(k, u) = -\Gamma_0 k^2 - k^4 + \frac{1}{2} \begin{cases} \kappa |\lambda_0| k^2, & \text{for } u = -1 \text{ if } \kappa \geq 1, \\ \kappa |\lambda_0| k^2, & \text{for } u = u^* \text{ if } 0 \leq \kappa < 1 \text{ and } k \leq k_c, \\ |\lambda_0| k^2 - 1, & \text{for } u = 1 \text{ if } 0 \leq \kappa < 1 \text{ and } k > k_c, \end{cases}$$

where $u^* = -1$ for $0 < \kappa < 1$ and is arbitrary for $\kappa = 0$, and $k_c = [|\lambda_0|(1 - \kappa)]^{-1/2}$. Note that this is identical to the corresponding expression presented in ref. [10], with λ_0 replaced by $|\lambda_0|$ and the roles of $u = 1$ and $u = -1$ switched. We thus find that the system may undergo one of three instabilities: an *isotropic* instability in which the dominant instability is independent of the direction ϕ , a *longitudinal instability* in which the most unstable mode points along the nematic director field ($\phi^* = \theta$), or a *transverse instability* in which it points perpendicular to the nematic director field ($\phi^* = \theta + \pi/2$).

The instability is driven by the wave number k for which $\sigma^*(k)$ is the largest, and the system is stable if $\sigma^*(k) < 0$ for all k . The analysis for $\lambda_0 < 0$ is identical to that presented for $\lambda_0 > 0$ in ref. [10], so we directly show the results in fig. 3. For the case $\kappa = 1$ considered in the main text, the stability boundary is given by the curve $|\lambda_0| = 2\Gamma_0/\kappa$ (fig. 3c), which corresponds to the pink curve in fig. 2a.

References

1. A.M. Turing, Philos. Trans. R. Soc. B **237**, 37 (1952).
2. M. Cross, H. Greenside. *Pattern Formation and Dynamics in Nonequilibrium Systems* (Cambridge University Press, Cambridge, 2009).
3. S. Taheri-Araghi, S.D. Brown, J.T. Sauls, D.B. McIntosh, S. Jun, Annu. Rev. Biophys. **44**, 123 (2015).
4. S.F. Gilbert, *Developmental Biology*, 8th edition (Sinauer Associates Inc., Sunderland, Massachusetts, USA, 2006).
5. J. Swift, P.C. Hohenberg, Phys. Rev. A **15**, 319 (1977).
6. N. Stoop, R. Lagrange, D. Terwagne, P.M. Reis, J. Dunkel, Nat. Mater. **14**, 337 (2015).
7. I.S. Aranson, L.S. Tsimring, Rev. Mod. Phys. **78**, 641 (2006).
8. H.H. Wensink, J. Dunkel, S. Heidenreich, K. Drescher, R.E. Goldstein, H. Löwen, J.M. Yeomans, Proc. Natl. Acad. Sci. U.S.A. **109**, 14308 (2012).
9. J. Dunkel, S. Heidenreich, K. Drescher, H.H. Wensink, M. Bär, R.E. Goldstein, Phys. Rev. Lett. **110**, 228102 (2013).
10. A.U. Oza, J. Dunkel, New. J. Phys. **18**, 093006 (2016).
11. Stephen J. DeCamp, Gabriel S. Redner, Aparna Baskaran, Michael F. Hagan, Zvonimir Dogic, Nat. Mater. **14**, 1110 (2015).
12. T. Sanchez, D.T.N. Chen, S.J. DeCamp, M. Heymann, Z. Dogic, Nature **491**, 431 (2012).
13. A. Czirók, T. Vicsek, Physica A **281**, 17 (2000).
14. H.H. Wensink, V. Kantsler, R.E. Goldstein, J. Dunkel, Phys. Rev. E **89**, 010302(R) (2014).
15. F. Peruani, A. Deutsch, M. Bär, Phys. Rev. E **74**, 030904 (2006).
16. F. Ginelli, F. Peruani, M. Bär, H. Chaté, Phys. Rev. Lett. **104**, 184502 (2010).
17. F.C. Keber, E. Loiseau, T. Sanchez, S.J. DeCamp, L. Giomi, M.J. Bowick, M.C. Marchetti, Z. Dogic, A.R. Bausch, Science **345**, 1135 (2014).
18. C. Dombrowski, L. Cisneros, S. Chatkaew, R.E. Goldstein, J.O. Kessler, Phys. Rev. Lett. **93**, 098103 (2004).
19. H.P. Zhang, A. Be'er, R.S. Smith, E.-L. Florin, H.L. Swinney, EPL **87**, 48011 (2009).
20. V. Schaller, C. Weber, C. Semmrich, E. Frey, A.R. Bausch, Nature **467**, 73 (2010).
21. L.H. Cisneros, J.O. Kessler, S. Ganguly, R.E. Goldstein, Phys. Rev. E **83**, 061907 (2011).
22. D.L. Koch, G. Subramanian, Annu. Rev. Fluid Mech. **43**, 637 (2011).
23. Y. Sumino, K.H. Nagai, Y. Shitaka, D. Tanaka, K. Yoshikawa, H. Chaté, K. Oiwa, Nature **483**, 448 (2012).
24. Kuo-An Liu, I. Lin, Phys. Rev. E **86**, 011924 (2012).
25. A. Sokolov, I.S. Aranson, Phys. Rev. Lett. **109**, 248109 (2012).
26. A. Zöttl, H. Stark, Phys. Rev. Lett. **112**, 118101 (2014).
27. I. Buttinoni, J. Bialké, F. Kümmel, H. Löwen, C. Bechinger, T. Speck, Phys. Rev. Lett. **110**, 238301 (2013).
28. M. Hennes, K. Wolff, H. Stark, Phys. Rev. Lett. **112**, 238104 (2014).
29. C.W. Wolgemuth, Biophys. J. **95**, 1564 (2008).
30. L. Giomi, M.C. Marchetti, T.B. Liverpool, Phys. Rev. Lett. **101**, 198101 (2008).
31. A. Baskaran, M.C. Marchetti, Proc. Natl. Acad. Sci. U.S.A. **106**, 15567 (2009).
32. S. Ramaswamy, Annu. Rev. Condens. Matter Phys. **1**, 323 (2010).

33. R. Großmann, P. Romanczuk, M. Bär, L. Schimansky-Geier, Phys. Rev. Lett. **113**, 258104 (2014).
34. A. Peshkov, I.S. Aranson, E. Bertin, H. Chaté, F. Ginelli, Phys. Rev. Lett. **109**, 268701 (2012).
35. D. Saintillan, M. Shelley, Phys. Fluids **20**, 123304 (2008).
36. D. Saintillan, M. Shelley, J. R. Soc. Interface **9**, 571 (2011).
37. M.C. Marchetti, J.F. Joanny, S. Ramaswamy, T.B. Liverpool, J. Prost, M. Rao, R.A. Simha, Rev. Mod. Phys. **85**, 1143 (2013).
38. P. Romanczuk, M. Bär, W. Ebeling, B. Lindner, L. Schimansky-Geier, Eur. Phys. J. ST **202**, 1 (2012).
39. P. Romanczuk, L. Schimansky-Geier, Phys. Rev. Lett. **106**, 230601 (2011).
40. R. Großmann, L. Schimansky-Geier, P. Romanczuk, New J. Phys. **14**, 073033 (2012).
41. J. Taktikos, V. Zaburdaev, H. Stark, Phys. Rev. E **85**, 051901 (2012).
42. H. Wioland, F.G. Woodhouse, J. Dunkel, J.O. Kessler, R.E. Goldstein, Phys. Rev. Lett. **110**, 268102 (2013).
43. E. Lushi, H. Wioland, R.E. Goldstein, Proc. Natl. Acad. Sci. U.S.A. **111**, 9733 (2014).
44. A. Kaiser, A. Peshkov, A. Sokolov, B. ten Hagen, H. Löwen, I.S. Aranson, Phys. Rev. Lett. **112**, 158101 (2014).
45. A. Kaiser, A. Sokolov, I.S. Aranson, H. Löwen, Eur. Phys. J. ST **224**, 1275 (2015).
46. J. Dunkel, S. Heidenreich, M. Bär, R.E. Goldstein, New J. Phys. **15**, 045016 (2013).
47. J. Toner, Y. Tu, Phys. Rev. Lett. **75**, 4326 (1995).
48. J. Toner, Y. Tu, Phys. Rev. E **58**, 4828 (1998).
49. J. Toner, Y. Tu, S. Ramaswamy, Ann. Phys. **318**, 170 (2005).
50. U. Frisch. *Turbulence* (Cambridge University Press, Cambridge, 2004).
51. S. Heidenreich, J. Dunkel, S.H.L. Klapp, M. Bär, Phys. Rev. E **94**, 020601(R) (2016).
52. R.H. Kraichnan, D. Montgomery, Rep. Prog. Phys. **43**, 547 (1980).
53. H. Kellay, W.I. Goldburg, Rep. Prog. Phys. **65**, 845 (2002).
54. R. Voituriez, J.F. Joanny, J. Prost, Phys. Rev. Lett. **96**, 028102 (2006).
55. N.S. Rossen, J.M. Tarp, J. Mathiesen, M.H. Jensen, L.B. Oddershede, Nat. Commun. **5**, 5720 (2014).
56. V. Bratanov, F. Jenko, E. Frey, Proc. Natl. Acad. Sci. U.S.A. **112**, 15048 (2015).
57. V. Narayan, S. Ramaswamy, N. Menon, Science **317**, 105 (2007).
58. I.S. Aranson, A. Snezhko, J.S. Olafsen, J.S. Urbach, Science **320**, 612 (2008).
59. S. Mishra, R.A. Simha, S. Ramaswamy, J. Stat. Mech.: Theor. Exp., P02003 (2010).
60. X.-Q. Shi, Y.-Q. Ma, Nat. Commun. **4**, 3013 (2013).
61. N. Goldenfeld, C. Woese, Annu. Rev. Condens. Matter Phys. **2**, 375 (2011).
62. A. Baskaran, M.C. Marchetti, Phys. Rev. E **77**, 011920 (2008).
63. T.C. Adhyapak, S. Ramaswamy, J. Toner, Phys. Rev. Lett. **110**, 118102 (2013).
64. Sumesh P. Thampi, Ramin Golestanian, Julia M. Yeomans, Phys. Rev. Lett. **111**, 118101 (2013).
65. L. Giomi, M.J. Bowick, X. Ma, M.C. Marchetti, Phys. Rev. Lett. **110**, 228101 (2013).
66. E. Putzig, G.S. Redner, A. Baskaran, A. Baskaran, Soft Matter **12**, 3854 (2016).
67. A. Doostmohammadi, M.F. Adamer, S.P. Thampi, J.M. Yeomans, Nat. Commun. **7**, 10557 (2016).
68. T. Gao, R. Blackwell, M.A. Glaser, M.D. Betterton, M.J. Shelley, Phys. Rev. Lett. **114**, 048101 (2015).
69. F.G. Woodhouse, R.E. Goldstein, Proc. Natl. Acad. Sci. U.S.A. **110**, 14132 (2013).
70. R.A. Simha, S. Ramaswamy, Phys. Rev. Lett. **89**, 058101 (2002).
71. P.G. de Gennes, J. Prost. *The Physics of Liquid Crystals*, Vol. **2** (Oxford University Press, Oxford, 1995).
72. C.P. Brangwynne, F.C. MacKintosh, S. Kumar, N.A. Geisse, J. Talbot, L. Mahadevan, K.K. Parker, D.E. Ingber, D.A. Weitz, J. Cell. Biol. **173**, 733 (2006).
73. V. Kantsler, R.E. Goldstein, Phys. Rev. Lett. **108**, 038103 (2012).
74. A.-K. Kassam, L.N. Trefethen, SIAM J. Sci. Comput. **26**, 1214 (2005).
75. P. Guillamat, J. Ignés-Mullol, S. Shankar, M.C. Marchetti, F. Sagués, arXiv:1606.05764 (2016).
76. L. Giomi, M.J. Bowick, P. Mishra, R. Sknepnek, M.C. Marchetti, Philos. Trans. R. Soc. A **372**, 20130365 (2014).
77. A. Sokolov, I.S. Aranson, J.O. Kessler, R.E. Goldstein, Phys. Rev. Lett. **98**, 158102 (2007).